

Metal-insulator transition and magnetism of SU(3) fermions in the square latticeEduardo Ibarra-García-Padilla ^{1,2,3,4,*}, Chunhan Feng ⁵, Giulio Pasqualetti,^{6,7,8} Simon Fölling ^{6,7,8},
Richard T. Scalettar ¹, Ehsan Khatami ² and Kaden R. A. Hazzard ^{3,4,1}¹*Department of Physics, University of California, Davis, California 95616, USA*²*Department of Physics and Astronomy, San José State University, San José, California 95192, USA*³*Department of Physics and Astronomy, Rice University, Houston, Texas 77005-1892, USA*⁴*Rice Center for Quantum Materials, Rice University, Houston, Texas 77005-1892, USA*⁵*Center for Computational Quantum Physics, Flatiron Institute, 162 5th Avenue, New York, New York 10010, USA*⁶*Ludwig-Maximilians-Universität, Schellingstraße 4, 80799 Munich, Germany*⁷*Max-Planck-Institut für Quantenoptik, Hans-Kopfermann-Straße 1, 85748 Garching, Germany*⁸*Munich Center for Quantum Science and Technology (MCQST), Schellingstraße 4, 80799 Munich, Germany*

(Received 20 June 2023; accepted 23 October 2023; published 13 November 2023)

We study the SU(3) symmetric Fermi-Hubbard model (FHM) in the square lattice at 1/3-filling using numerically exact determinant quantum Monte Carlo and numerical linked-cluster expansion techniques. We present the different regimes of the model in the T - U plane, which are characterized by local and short-range correlations, and capture signatures of the metal-insulator transition and magnetic crossovers. These signatures are detected as the temperature scales characterizing the rise of the compressibility, and an interaction-dependent change in the sign of the diagonal spin-spin correlation function. The analysis of the compressibility estimates the location of the metal-insulator quantum critical point at $U_c/t \sim 6$, and provides a temperature scale for observing Mott physics at finite T . Furthermore, from the analysis of the spin-spin correlation function we observe that for $U/t \gtrsim 6$ and $T \sim J = 4t^2/U$ there is a development of a short-range two-sublattice (2SL) antiferromagnetic structure, as well as an emerging three-sublattice (3SL) antiferromagnetic structure as the temperature is lowered below $T/J \lesssim 0.57$. This crossover from 2SL to 3SL magnetic ordering agrees with Heisenberg limit predictions, and has observable effects on the density of on-site pairs. Finally, we describe how the features of the regimes in the T - U plane can be explored with alkaline-earth-like atoms in optical lattices with currently achieved experimental techniques and temperatures. The results discussed in this paper provide a starting point for the exploration of the SU(3) FHM upon doping.

DOI: [10.1103/PhysRevA.108.053312](https://doi.org/10.1103/PhysRevA.108.053312)**I. INTRODUCTION**

The study of Fermi-Hubbard models (FHM) with spin $S > 1/2$ and higher SU($N > 2$) symmetries has gained interest in recent years due to the interesting exotic ground states they are predicted to display, their relevance to multiorbital materials, and their precise realization in ultracold atoms. Their richness is exemplified in the Heisenberg limit, where the density is on average one particle per site ($\langle n \rangle = 1$) and the repulsive on-site interaction energy dominates over the tunneling amplitude ($U \gg t$). Already in this simplifying limit, the model on the two-dimensional (2D) square lattice is predicted to exhibit a plethora of ground states with a complicated N dependence [1–7].

The possibility to experimentally explore the rich phase diagram of the SU(N) FHM is opened by the rapid development of quantum simulation capabilities with alkaline-earth-like atoms (AEAs) in optical lattices (OLs). Due to the intrinsic SU(N) nuclear spin symmetry of fermionic AEAs (such as ^{173}Yb and ^{87}Sr) [8–12], experiments can engineer the SU(N)

FHM with N tunable from 2, 3, . . . , 10. In the past few years, experiments with ^{173}Yb in OLs have explored the SU(N) FHM for different values of N and in different geometries: In the three-dimensional (3D) cubic lattice, they have studied the Mott insulator state for $N = 6$ [13], the equation of state for $N = 3, 6$ [14], and a flavor-selective Mott insulator for $N = 3$ [15]. In 2D dimerized OLs, experiments have measured nearest-neighbor antiferromagnetic (AFM) correlations for $N = 4$ [16]. In 1D, 2D, and 3D hypercubic lattices with uniform tunneling rates, nearest-neighbor AFM correlations have been detected for $N = 6$ [17]. The future implementation of quantum gas microscopy for two-dimensional OLs realizing the SU(N) FHM [18–26] is expected to reveal a wealth of physics as it will allow for the characterization of finite-temperature analogs of a variety of proposed ground states via the direct observation of site-resolved spin-spin correlations [17,27–29]. These experimental efforts call for a thorough theoretical understanding of the phase diagrams for $N > 2$, and in particular, finite-temperature signatures of their rich physics.

A question of interest in the SU(N) FHM occurs at $1/N$ -filling ($\langle n \rangle = 1$) in the 2D square lattice. At this filling, the $N > 2$ FHM provides us with the opportunity to disentangle

*edibarra@ucdavis.edu

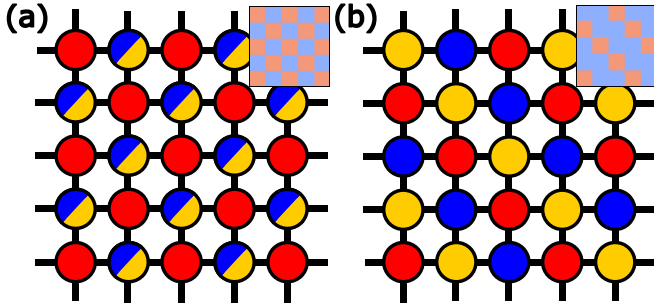


FIG. 1. Schematics of magnetic orderings. (a) 2SL AFM. Here the ordering wave vector is $(\pm\pi, \pm\pi)$, where in sublattice A there is a predominance of a spin flavor and in sublattice B there is a spin with a different flavor (a superposition of the other two spin flavors). (b) 3SL AFM. Here the ordering wave vector is $(\pm 2\pi/3, \pm 2\pi/3)$ and in this case, spins of the same flavor alternate every three sites. The insets correspond to the sign of $C(\vec{r})$ in Eq. (5), measured from the site in the lower left corner, for the ideal arrangements shown. Orange (blue) corresponds to a positive (negative) sign.

the role played by nesting and Mott physics since, in contrast to SU(2), a finite U is required to open a charge gap. While the SU(2) FHM at 1/2-filling exhibits perfect nesting of the Fermi surface and a van Hove singularity in the density of states, the $N > 2$ counterparts achieve $\langle n \rangle = 1$ without these special band structure features and allow us to separate band structure attributes from the effect played by interactions without the need to consider next-nearest-neighbor tunneling amplitudes t' , which are hard to control in ultracold atom experiments.

In this work, we focus on $N = 3$, for which the model is predicted to display interesting physical phenomena even in very special limits and geometries [30–38]. For example, in the 2D square lattice in the weak-coupling regime, mean-field theory and renormalization group calculations predict that the ground state is an SU(3) symmetry breaking phase at half-filling ($\langle n \rangle = 1.5$) [39]. Moreover, at 1/3-filling ($\langle n \rangle = 1$), our focus in this paper, exact diagonalization, density-matrix renormalization group, and infinite projected entangled-pair states calculations find that the ground state in the Heisenberg limit exhibits a 3SL AFM ordering [2,3]. This finding is corroborated by high-temperature series expansions and large-scale exact diagonalization calculations in Ref. [40], which further suggest the existence of a short-range 2SL AFM ordering prior to the onset of the 3SL AFM ordering as the temperature is lowered. Furthermore, approximate techniques, such as dynamical mean-field theory, predict such change in the magnetic ordering also occurs in the Hubbard regime [30,31] (see Fig. 1 for schematics of the magnetic orderings).

Here, we study the SU(3) FHM on the square lattice at 1/3-filling, using numerically exact finite-temperature determinant quantum Monte Carlo (DQMC) [41,42] and numerical linked-cluster expansion (NLCE) techniques [43,44]. We explore experimentally accessible quantities such as the compressibility, the density of on-site pairs, and the spin-spin correlation functions as a function of temperature and interaction strength ($U/t \in [0.5, 12]$). These quantities display finite-temperature signatures of the metal-insulator transition at $U_c/t \sim 6$, and capture the evolution of the magnetic ordering from 2SL to

3SL for $U > U_c$, which allows us to propose a phase diagram where we present regions with different characteristic behaviors of the model in the $T-U$ space. It is important to note that these regions are not distinct phases and that boundaries correspond to crossovers characterized by short-range correlations rather than phase transitions. For example, we note the metal-insulator transition that occurs at $T = 0$ and is accompanied by the presence of a long-range magnetic ordering. However, at finite- T the Mermin-Wagner theorem prohibits the spontaneous symmetry breaking and therefore only short-range spin correlations are present. This work provides experimentally accessible signatures of the metal-insulator transition and magnetic crossovers in the SU(3) FHM in the 2D square lattice.

The remainder of the paper is organized as follows. In Sec. II, we present the SU(3) FHM Hamiltonian, the observables we measure, and the details of the numerical techniques used. In Sec. III, we present the main results of the paper, and in Sec. IV we present our conclusions.

II. MODEL AND METHODS

The Hamiltonian for the SU(3) FHM is

$$H = -t \sum_{\langle i,j \rangle, \sigma} (c_{i\sigma}^\dagger c_{j\sigma} + \text{H.c.}) + \frac{U}{2} \sum_{i, \sigma \neq \tau} n_{i\sigma} n_{i\tau} - \mu \sum_{i, \sigma} n_{i\sigma}, \quad (1)$$

where $c_{i\sigma}^\dagger$ ($c_{i\sigma}$) is the creation (annihilation) operator for a fermion with spin flavor $\sigma = 1, 2, 3$ on site $i = 1, 2, \dots, N_s$ in a 2D square lattice, N_s denotes the number of lattice sites, $n_{i\sigma} = c_{i\sigma}^\dagger c_{i\sigma}$ is the number operator for flavor σ on site i , and μ is the chemical potential that controls the fermion density. We work in units where $k_B = 1$ throughout the paper.

We are interested in thermodynamic quantities and correlation functions. We focus on the density

$$\langle n \rangle = \frac{1}{N_s} \sum_{i, \sigma} \langle n_{i\sigma} \rangle, \quad (2)$$

the isothermal compressibility

$$\kappa = \frac{1}{\langle n \rangle^2} \frac{d\langle n \rangle}{d\mu}, \quad (3)$$

the density of on-site pairs

$$\mathcal{D} = \frac{1}{N_s} \sum_i \left[\frac{1}{2} \sum_{\sigma \neq \tau} \langle n_{i\sigma} n_{i\tau} \rangle \right], \quad (4)$$

and the real-space spin-spin connected correlation functions

$$C(\vec{r}) = \frac{1}{N_s} \sum_{\vec{r}_0} \left[\sum_{\sigma \neq \tau} (\langle n_{\vec{r}_0, \sigma} n_{\vec{r}_0 + \vec{r}, \sigma} \rangle - \langle n_{\vec{r}_0, \sigma} \rangle \langle n_{\vec{r}_0 + \vec{r}, \tau} \rangle) \right], \quad (5)$$

where \vec{r}_0 runs through all the lattice vectors in the lattice. The sign of this function is shown for the schematic 2SL and 3SL orders in the insets of Fig. 1: for the 2SL, the sign alternates in a checkerboard pattern, while in the 3SL the sign changes every two blocks in the Manhattan distance [45].

The above observables provide valuable knowledge about the physics of the model: the compressibility and the density of on-site pairs are useful measures of the degree to which the

system is a Mott insulator, while the spin correlation functions detect magnetic ordering, and as we will see below, capture important information about the nature of the transition.

In practice, at each U/t and T/t the average density is fixed to $\langle n \rangle = 1.000 \pm 0.006$. In the calculation of derivatives in DQMC, we used the three-point differentiation rule [46]. In the case of the compressibility, the derivative is taken first and then linearly interpolated with respect to the density to obtain κ at the target density. For NLCE, the compressibility is computed using the fluctuation dissipation theorem $\frac{d\langle n \rangle}{d\mu} = \frac{1}{T}[\langle n^2 \rangle - \langle n \rangle^2]$, where $\langle n^2 \rangle = \frac{1}{N_s^2} \sum_{i,j} \langle n_i n_j \rangle$ and $n_i = \sum_{\sigma} n_{i\sigma}$. Since $\langle n \rangle = 1$ throughout the paper, we drop the prefactor $1/\langle n \rangle^2$ in κ for simplicity.

Observables in thermal equilibrium are obtained using DQMC and NLCE. DQMC and NLCE are often the exact and complementary numerical methods of choice for the SU(2) FHM at the finite temperatures relevant to ultracold matter [46–52]. Here, we use our extension of DQMC and NLCE for SU(N) systems [17,33]. Generally speaking, the DQMC performs best at weak to intermediate interactions, while the NLCE performs best at strong interactions; we present results from both methods where they are viable. For the temperatures and interaction strengths where NLCE and DQMC are well converged, the methods agree well, supporting the validity of our results.

A. Determinant quantum Monte Carlo

In this method, a path integral for the partition function is obtained by discretizing the inverse temperature β in steps of $\Delta\tau$, i.e., $\beta = L\Delta\tau$. We use a Trotter step $\Delta\tau = 0.05/t$. We introduce three auxiliary Hubbard-Stratonovich (HS) fields to decouple each interaction term and integrate out the fermionic degrees of freedom. We then sample the HS fields stochastically. In order to obtain accurate results, we obtain DQMC data for 40–60 different random seeds for each of the T/t and U/t considered. For each Monte Carlo trajectory we perform 2000 warmup sweeps and 8000 sweeps for measurements. The number of global moves per sweep to mitigate possible ergodicity issues [53] is set to 4 [54].

We analyze the systematic errors (finite-size and Trotter errors) at $T/t \leq 1$ (see Appendixes B and C). To estimate finite-size effects, we perform calculations using 6×6 , 8×8 , and 12×12 lattices at interaction strengths above and below the quantum critical point. We find that when significant, these are inconsequential to the main conclusions of the paper. Hence, unless explicitly stated, we draw our conclusions based on results on the 6×6 lattice due to computational cost (see Sec. III and Appendix B). Finally, we estimate Trotter errors at large interaction strengths. These are presented in Appendix C, and do not affect the main conclusions of the paper.

B. Numerical linked cluster expansion

In the NLCE, extensive properties of the lattice model in the thermodynamic limit are expressed as sums of contributions from all topologically distinct clusters, up to a certain size, that can be embedded in the lattice. Those contributions are in turn calculated exactly using full diagonalization of the

model Hamiltonian on the finite clusters. See Ref. [44] for details. We use spin flavor conservation symmetry to block diagonalize the Hamiltonian matrix of each cluster [33], which allows us to perform the calculations up to seven orders in a site expansion (considering all clusters up to seven sites) for thermodynamic quantities, and up to six orders for correlation functions.

To compute correlation functions beyond nearest neighbors, one needs to work with not only the topologically distinct clusters for a model involving only nearest-neighbor hopping, but rather all clusters that can be embedded on the lattice and are not related by translation or point-group symmetry operations. The number of the latter is significantly higher than the number of topologically distinct clusters and puts a severe constraint on time in our calculations.

The NLCE is an expansion directly in the thermodynamic limit, and its accuracy is controlled by the order (no statistical or systematic errors are present when the series is converged). We show the two highest orders and only show data for regions where the two highest orders agree within 1%.

III. RESULTS

The results section is organized as follows: We first present the T - U diagram of the SU(3) FHM, which summarizes our findings. This is followed by discussions of the compressibility, which illustrates finite-temperature signatures of the metal-insulator transition. Then we analyze the spin-spin correlations, which capture the development of the short-range 2SL AFM structure, and the change in the magnetic ordering from 2SL to 3SL. Finally we argue that this change in the magnetic ordering has observable effects in the density of on-site pairs.

The main results of the paper are summarized in Fig. 2. The regions shown do not represent long-range ordered phases, but instead correspond to our findings appertaining the development of short-range correlations in the model in the T - U space. We will describe them here, and then describe in the rest of the paper how these conclusions were obtained. We detect finite- T signatures of a metal-insulator quantum phase transition ($T = 0$) consistent with a critical interaction of $U_c/t \sim 6$ (red star) by studying the compressibility. This finding is also consistent with ground-state calculations using constrained path quantum Monte Carlo (CPQMC), which also predicts $U_c/t \sim 5.5$ (yellow star) [55]. From the spin-spin correlation functions we observe that for $U \gtrsim U_c$ and $T \sim J$ ($J = 4t^2/U$ is the antiferromagnetic exchange energy) a short-range 2SL AFM structure develops and is manifest in spin correlations of about 2% of their maximal allowed values at relatively high temperatures of $T/t \sim 0.6$. While a fairly small value in absolute terms, correlations of this magnitude are now routinely probed in quantum gas microscope experiments [24–26]. Furthermore, we detect in the density of on-site pairs and the spin-spin correlation function that as the temperature is lowered below $T/J \sim 0.57$, the system starts developing a 3SL AFM order. It is worth mentioning that this change from 2SL to 3SL ordering is consistent with the observations in the Heisenberg limit [40], which also predict the appearance of an emerging 3SL order, albeit at a lower temperature of $T/J \sim 0.15$. The apparent discrepancy in

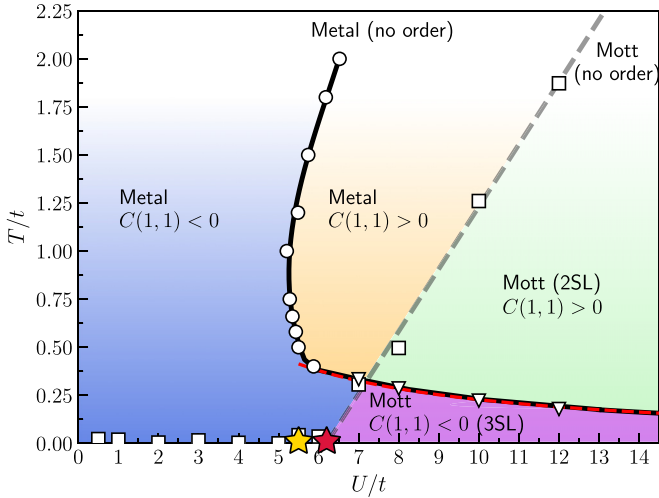


FIG. 2. Regimes of the SU(3) Fermi-Hubbard model in the two-dimensional square lattice. Squares indicate $T = \Delta$ obtained from the compressibility [see Fig. 3 and Eq. (6)]. Circles correspond to the zero crossing of the next-nearest-neighbor spin correlator $C(1, 1)$ [see Fig. 4]. Triangles correspond to the location of the dip in dP/dT [see Fig. 6] (also $C(1, 1)$ exhibiting a zero crossing [see Fig. 5]). The black line indicates the $C(1, 1) = 0$ curve. The model exhibits a metal-insulator transition at $U_c/t \sim 6$ at $T = 0$ [red star: this work, yellow star: CPQMC (see main text)], and crossovers at finite T indicated by the black and gray lines. For $U \geq U_c$ and at $T \lesssim 0.3(U - U_c)$ the system is a Mott insulator, and develops a short-range 2SL AFM structure from a metallic phase at $T \sim J$. As the temperature is lowered, below $T/J \sim 0.57$, the system starts developing a 3SL AFM order (the dashed red line corresponds to the $T/J = 0.57$ curve). We use a qualitative color fading scheme at high temperatures to indicate the disappearance of magnetic correlations.

relevant temperatures arises from the fact that the study in the Heisenberg limit considers the evolution of the structure factor (which signals longer-range correlations), whereas here we discuss the crossover temperature, where the appropriate sign of the diagonal spin correlations appear. That is, we focus on the onset of the shortest distance correlations becoming consistent with the magnetic ordering. Naturally, this crossover temperature is expected to be higher than the temperature where the structure factor at $(\pm 2\pi/3, \pm 2\pi/3)$ surpasses the one at $(\pm\pi, \pm\pi)$.

The first natural quantity to look at as a measure of the Mott insulating nature of the system is the compressibility $\kappa = d\langle n \rangle / d\mu$, which is presented in Fig. 3. Here we show κ as a function of T/t for different values of U/t from DQMC (symbols) and NLCE (dotted and solid lines), which show a good agreement in their common regions of validity. For $U/t \lesssim 4$, κ is large and the system is highly compressible, characteristic of a metal. In contrast, for $U/t \gtrsim 7$ the compressibility does not rise as strongly with increasing temperature around $T \lesssim U$ and remains small for all T/t . Finally, the intermediate region $4 \lesssim U/t \lesssim 7$ is the most interesting one as it illustrates a qualitatively different behavior as T/t is lowered: instead of reaching a peak and then decreasing with decreasing T , it remains roughly flat for about a decade in temperature ($0.2 \lesssim T \lesssim 2$). It is worth noting that at these temperatures and interactions, the flatness of the

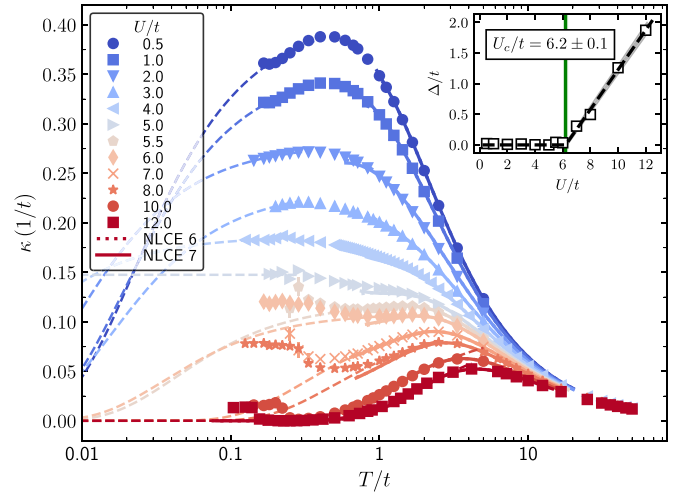


FIG. 3. Compressibility as function of T/t for different U/t and the Mott gap as a function of U/t . Markers correspond to DQMC calculations, dotted and solid lines correspond to the last two NLCE orders computed, and dashed lines are the fits to $ae^{-\Delta/T}$ to extract $\Delta(U)$. Inset: Δ/t as a function of U/t . The dashed line is obtained by fitting to Eq. (6) and indicates the location of $U_c/t = 6.2 \pm 0.1$ for the metal-insulator transition.

compressibility also coincides with the almost temperature-independent location of the $C(1, 1) = 0$ boundary in Fig. 2 (denoted by circles, see further discussion below).

We can distill physically salient information from this data by following the analysis performed in Refs. [56,57] for the triangular lattice SU(2) Hubbard model. There, for a given U/t , the data is fitted using $\kappa = ae^{-\Delta/T}$ (where Δ is the charge gap) in the temperature window where κ exhibits a non-negative slope. These fits are indicated as dashed lines in Fig. 3 and allow us to extract $\Delta(U)$, which we then plot as a function of U/t (see inset in Fig. 3). These results show that the system is metallic below $U/t \sim 6$ and insulating above it, with a linear dependence in U/t as expected. To extract the quantum critical point from this technique we perform the following fit:

$$\Delta = \begin{cases} 0 & \text{if } U < U_c \\ b(U - U_c) & \text{if } U > U_c \end{cases}, \quad (6)$$

for which we obtain the parameters $b = 0.32 \pm 0.01$, and $U_c = 6.2 \pm 0.1$ [58].

Finally, it is worth mentioning that the range of temperatures included in the fit over T/t at fixed U/t omits the temperatures below the upturn in κ at the lowest T/t for $U/t > 6$, which occurs at the same temperature scale where \mathcal{D} exhibits a sharp upturn and is related to a change in the magnetic ordering (see Fig. 6 and its discussion for more details).

At $T = 0$ the gap opening may coincide with the magnetic ordering transition, however, at finite temperatures these may behave differently. To investigate this, Fig. 4 presents the spin-spin correlations as a function of U/t for different T/t . Figure 4(a) shows the nearest-neighbor spin correlation $C(1, 0)$, which highlights the agreement between DQMC and NLCE. We first note that $C(1, 0) < 0$ for all values of U/t .

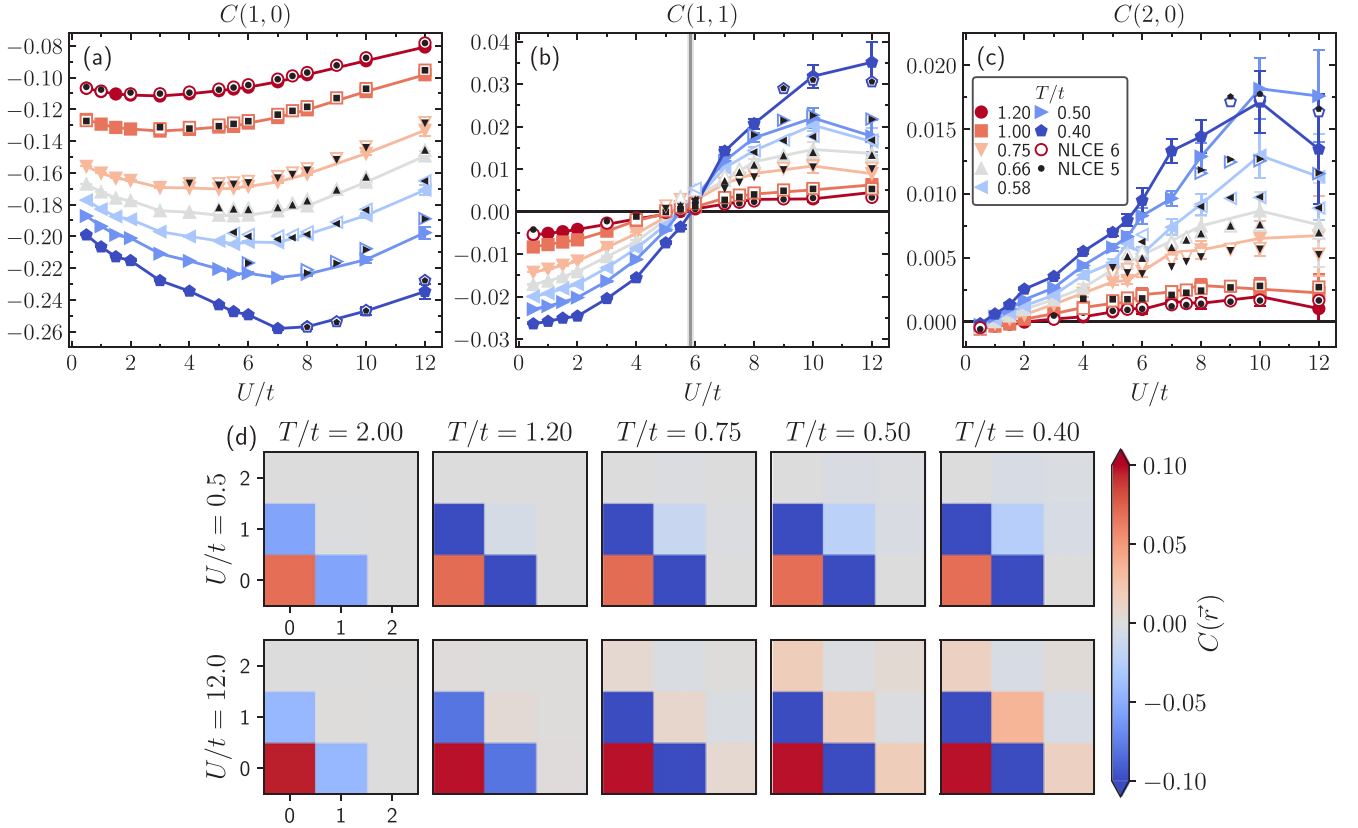


FIG. 4. Spin-spin correlations. Results are presented as a function of U/t for different T/t for the (a) nearest-neighbor $C(1, 0)$, (b) next-nearest-neighbor $C(1, 1)$, and (c) third neighbor $C(2, 0)$. (d) Examples of real-space spin correlations for $U/t = 0.5$ and $U/t = 12$ at different temperatures, which illustrate the metallic behavior of the system at small U/t , and the development of short-range 2SL correlations for large U/t . Here the on-site correlator $C(0, 0) = 2\langle n \rangle - 2D$ is rescaled by a factor of $1/20$ so its dependence on temperature and interaction strength is more clear. In (a)–(c) filled color symbols correspond to DQMC, and NLCE results from order 6 (order 5) are shown as open (black) markers. Results in (d) correspond to DQMC calculations. In all panels DQMC results were obtained on 6×6 lattices. The circles in Fig. 2 are obtained by locating the crossing $U^*(T)$ of $C(1, 1)$ vs U/t at fixed T/t after linear interpolation. The gray line in (b) is a guide to the eye of the location of $U^*(T)$ for the temperatures presented.

As temperature is lowered, the AFM nearest-neighbor correlations increase for all U/t , being strongest around $U/t \sim 7$ for the lowest temperatures. At the lowest temperatures, the shape of $C(1, 0)$ with U/t can be understood as follows: Starting from the noninteracting limit, as one increases U/t , local moment formation will lead to the development of stronger AFM nearest-neighbor correlations; however, when increasing U/t in the strong-coupling region, the relevant energy scale becomes the superexchange energy, $J = 4t^2/U$, and thus the correlations decrease for larger U/t at fixed T/t .

The next-nearest-neighbor spin correlator $C(1, 1)$ exhibits a distinctive U/t dependence [Fig. 4(b)], where again results from the two methods agree. At temperatures above $T/t \geq 2$, $C(1, 1)$ vanishes for all U/t considered and no order is expected [see, for example, Fig. 4(d)]. As the temperature is lowered, the correlations increase in magnitude and at each temperature a zero crossing occurs at $U^*(T)$ (indicated with circles in Fig. 2), i.e., $C(1, 1) < 0$ for $U < U^*(T)$ and changes sign for $U > U^*(T)$. This phenomenon is reminiscent of the doped $SU(2)$ FHM on square lattices where $C(1, 1)$ changes sign upon doping at a fixed T/t and U/t [49]. In the $SU(2)$ case $C(1, 1) < 0$ indicates metallic behavior as it reflects the effects of Pauli blocking, a signature of noninteracting

fermions. In our case, the change in sign of $C(1, 1)$ reflects a combination of Pauli blocking (dominant at $U < U^*$) and interaction-driven superexchange physics ($U > U^*$).

Figure 4(c) illustrates the third-neighbor spin correlation function $C(2, 0)$. We find $C(2, 0) > 0$ for most values of U/t shown (generally stronger for larger values of U/t), and it increases in magnitude as the temperature is lowered. The positive sign of the correlator is in agreement with the sign of the spin correlator in the 2SL ordering [see inset in Fig. 1(a)]. We attribute the disagreement of DQMC results at $T/t \leq 0.5$ in the strong-coupling region with the converged NLCE results to systematic errors in the DQMC, especially the finite-size error for this longer-range correlation function. Finally, Fig. 4(d) presents the real-space spin-spin correlation functions for $U/t = 0.5$ and $U/t = 12$ for different T/t . As the temperature is lowered, the system develops stronger nearest-neighbor AFM correlations for both U/t , and for $T/t = 1.2$ the sign change of $C(1, 1)$ is already evident. As the temperature is lowered even further, the system at weak U/t remains metallic, but at strong U/t displays a short-range 2SL AFM order in agreement with the Heisenberg limit predictions [40]. It is important to point out that the study of the nature of the underlying 2SL structure is an interesting question that

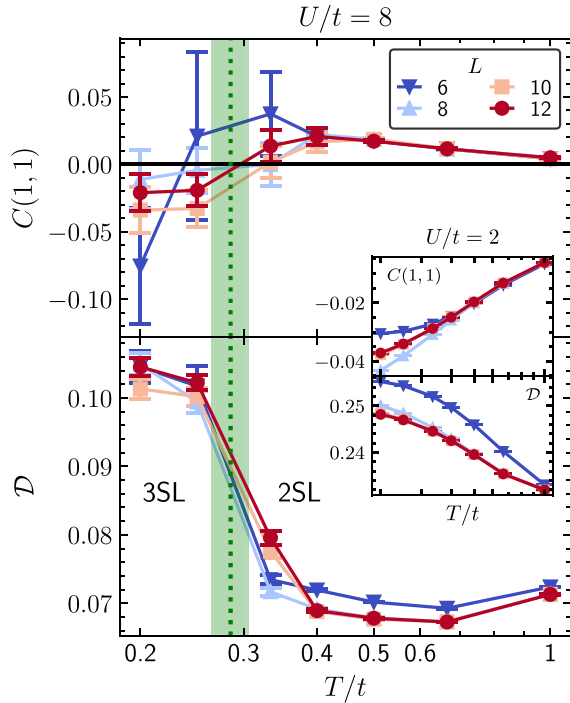


FIG. 5. Finite-size analysis. $C(1, 1)$ and \mathcal{D} as a function of T/t are presented for $U/t = 8$ ($U/t = 2$ in the inset) at system sizes: 6×6 , 8×8 , 10×10 , and 12×12 . Dotted vertical line corresponds to $T = 0.57J$, and the shaded region is half the spacing between the middle point of the two consecutive markers. Horizontal scale of the inset is the same as the main figure.

requires further exploration, and we expect future studies to be able to resolve it by analyzing correlation functions of the order parameters derived from the Gell-Mann matrices (see Ref. [30] for a discussion).

Systematic calculations of $C(1, 1)$ for different system sizes further support the claim of the change in sign observed in Fig. 4(b) for $T/t \geq 0.4$. This is illustrated in the top panels of Fig. 5 where we show results for $U/t = 8$ (main panel) and $U/t = 2$ (inset) as a function of T/t for different system sizes $L \times L$. As the temperature is lowered below $T/t < 0.4$ we observe that for $U/t = 8$ finite-size errors are severe for 6×6 lattice. However, results for $L \geq 8$ point to the same behavior: they all display a zero crossing in the temperature window $0.25 < T/t < 0.33$. Moreover, results for the two largest system sizes, 10×10 and 12×12 , agree with each other within the error bars and make clear that $C(1, 1)$ is negative at the lowest two temperatures and positive for the rest. For these system sizes, we compute the correlation function at the three lowest temperatures for $U/t = 8$ using 160 independent runs to improve the statistics. We identify this change in sign at lower temperatures as the temperature scale at which the change in ordering from 2SL to 3SL occurs (see insets in Fig. 1, which illustrate the sign of the spin correlation function for both orderings). In contrast, for $T/t < 0.4$ and $U/t = 2$, despite the presence of finite-size errors in 6×6 and 8×8 lattices, results for the two largest system sizes are consistent with each other and remain negative.

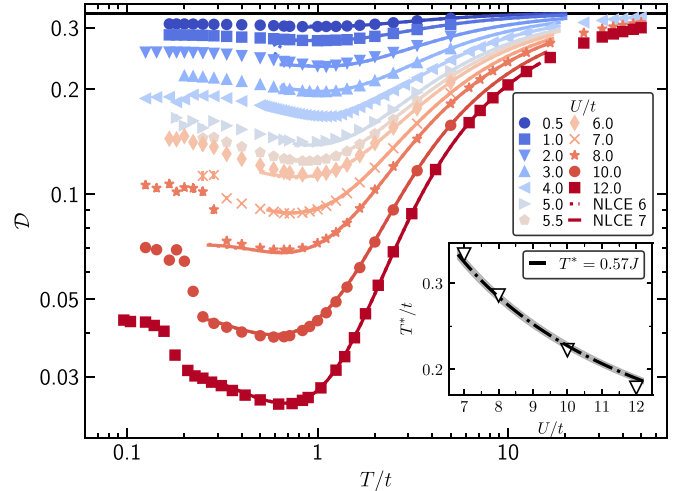


FIG. 6. Density of on-site pairs. DQMC (markers) and NLCE (lines) results are presented as a function of T/t for different U/t for the density of on-site pairs \mathcal{D} . The horizontal black line at $\mathcal{D} = 1/3$ corresponds to the $U = 0$ limit. The inset presents the behavior of T^*/t as a function of U/t , where T^*/t are obtained by locating the minima of $d(U\mathcal{D})/dT$ for $U/t > 5$. The data are fitted to $T^* = (0.57 \pm 0.01)J$.

This change in sign in $C(1, 1)$ as a function of temperature coincides with the low-temperature rise in the density of on-site pairs \mathcal{D} for $U/t = 8$ as evidenced in the bottom panel of Fig. 5. For $U/t = 8$, the finite-size error in \mathcal{D} is minimal at all temperatures considered in 6×6 lattices, and the location of the pronounced upturn remains consistent across all system sizes. For comparison, for $U/t = 2$ there is a finite-size error in \mathcal{D} , but it does not change the smooth temperature dependence of \mathcal{D} as demonstrated by calculations on 12×12 lattices, which agree with the 6×6 results (see bottom inset in Fig. 5).

These findings allow us to conclude that the change in the magnetic ordering from 2SL to 3SL, as evidenced by the change in sign of $C(1, 1)$ for $U > U_c$, has observable effects in the density of on-site pairs: the temperature scale at which the upturn in \mathcal{D} occurs coincides with that of the zero crossing. This connection between \mathcal{D} and the change in magnetic ordering motivates our next analysis.

Unlike the correlation function $C(1, 1)$, \mathcal{D} exhibits minimal finite-size errors. The low-temperature upturn can also be captured using less statistics, and hence requires less computational resources, than that needed to resolve the 2SL to 3SL magnetic crossover using $C(1, 1)$. In Fig. 6, we show the density of on-site pairs \mathcal{D} as a function of T/t for different values of U/t , which displays several familiar trends as well as the novel low-temperature feature. As expected, larger U/t lead to smaller overall \mathcal{D} , and as the temperature initially decreases, \mathcal{D} is suppressed from its high-temperature value around $T \sim U$. Following the development of antiferromagnetic correlations in the system below a temperature of the order of J , \mathcal{D} slowly rises again upon further lowering the temperature. That is because the probability of finding a particle with a different flavor at, and therefore virtual hoppings to, neighboring sites increases.

In addition to the above increase, we observe the remarkably sharp upturn in \mathcal{D} at even lower temperatures for $U > U_c$ only. As previously discussed, we attribute this behavior to a magnetic reordering of spins from the 2SL to the 3SL ordered phases. The inset in Fig. 6 presents the location T^*/t vs U/t , where T^*/t is defined as the temperature at which the minima of $d(P = U\mathcal{D})/dT$ is located, namely, the temperature where the upturn of \mathcal{D} upon lowering T is the largest (see Fig. 7 in the Appendix for the plot of dP/dT vs U/t) and corresponds to the change in magnetic ordering. We then fit the points to $T^* = aJ$, with $a = 0.57 \pm 0.01$. It is important to point out that this phenomenon survives the extrapolation $\Delta\tau \rightarrow 0$, as illustrated in Fig. 9 of Appendix C, and finite-size scaling as shown in Fig. 5. On the other hand, the NLCE results do not capture this phenomenon as the lowest convergence temperatures are typically above the onset of this sharp upturn.

IV. DISCUSSION AND OUTLOOK

We have explored the behavior of the SU(3) FHM in the square lattice at 1/3-filling as a function of U/t and T/t using complementary QMC and NLCE methods. We computed the compressibility, the density of on-site pairs, and the spin-spin correlation functions, which are experimentally accessible with ultracold AEAs in OLs. These quantities express finite-temperatures signatures of a quantum metal-insulator transition, which we locate at $U_c/t \sim 6$, and capture the temperature scale where the magnetic ordering evolves from a short-range 2SL to a 3SL for $U > U_c$ at $T/J \sim 0.57$.

These results imply the existence of different regimes of the model in the T - U plane, which are accessible in current experiments with AEAs in a 2D OL. First, the compressibility can be computed by measuring the equation of state $\langle n(\mu, U, T) \rangle$ and taking the derivative of $\langle n \rangle$ with respect to μ [14]. Furthermore, local access to the density in SU(N) systems [59] allows experiments to probe the density fluctuations, and therefore extract the temperature, since these are related to the compressibility via the fluctuation dissipation theorem [25,60]. Second, the density of on-site pairs can be measured using a photoassociation technique [14,16,17], which can be used to locate T^* . Finally, $C(1, 1)$ can be directly measured with an AEA quantum gas microscope. The low temperatures of some features seen here present some challenge, but combining the temperatures already achieved in Ref. [17] with local imaging should allow experiments to observe most of the phenomena presented in Fig. 2.

In fact, the key quantities to see the physics described in this paper can be measured without a full quantum gas microscope, as long as local resolution is good enough to measure the density and its fluctuations, as has been demonstrated for SU(N) AEA systems very recently [59]. We discuss a protocol for this here: the idea is to relate spin fluctuations in a small region W set by the imaging resolution to number fluctuations using a shelving scheme, and then relate the spin fluctuations to correlations within the region W .

The idea is to remove or shelve spin components, e.g., by using the 578 nm narrow clock transition in ^{173}Yb , and measure the density fluctuations of the remaining ground-state atoms. First note that the total particle number measured in a region W is $n_W = \sum_{j \in W} n_j$ (where $n_j = \sum_{\sigma} n_{j\sigma}$), and the

averaged fluctuations of this quantity, \mathcal{C} are

$$\mathcal{C} = \langle n_W^2 \rangle - \langle n_W \rangle^2 \quad (7)$$

$$= \left\langle \left(\sum_{j \in W} n_j \right)^2 \right\rangle - \left\langle \sum_{j \in W} n_j \right\rangle^2 \quad (8)$$

$$= \sum_{i, j \in W} (\langle n_i n_j \rangle - \langle n_i \rangle \langle n_j \rangle) \quad (9)$$

$$= \sum_{i, j \in W; \sigma \tau} [\langle n_{i\sigma} n_{j\tau} \rangle - \langle n_{i\sigma} \rangle \langle n_{j\tau} \rangle]. \quad (10)$$

Hence we see the number fluctuations in W are related in a simple way to the correlations.

Equation (10) can be used to relate density fluctuations to spin correlations by shelving M of the N components (any $0 < M < N$ suffices) to states that are not imaged. Using $\langle \dots \rangle$ to represent expectations in the preshelved state (which we want to know) and $\langle \dots \rangle_{\text{shelved}}$ for expectations in the shelved state, we obtain for the density fluctuations after shelving

$$\mathcal{C}^{(M)} = \sum_{i, j \in W; \sigma \tau} [\langle n_{i\sigma} n_{j\tau} \rangle - \langle n_{i\sigma} \rangle \langle n_{j\tau} \rangle]_{\text{shelved}} \quad (11)$$

$$= \sum_{i, j \in W; \sigma \tau \in \text{unshelved}} [\langle n_{i\sigma} n_{j\tau} \rangle - \langle n_{i\sigma} \rangle \langle n_{j\tau} \rangle]. \quad (12)$$

The second line follows because if spin component ν is shelved, any terms involving $n_{i\nu}$ vanish while unshelved states are unaltered. Using the permutation symmetry of the spin components,

$$\mathcal{C} = N \sum_{i, j \in W} [\langle n_{i\sigma} n_{j\sigma} \rangle + (N-1) \langle n_{i\sigma} n_{j\tau \neq \sigma} \rangle - N \langle n_{i\sigma} \rangle^2] \quad (13)$$

$$\mathcal{C}^{(M)} = M \sum_{i, j \in W} [\langle n_{i\sigma} n_{j\sigma} \rangle + (M-1) \langle n_{i\sigma} n_{j\tau \neq \sigma} \rangle - M \langle n_{i\sigma} \rangle^2] \quad (14)$$

and the sum of the spin-spin correlation function [defined in Eq. (5)] in region W is therefore:

$$\tilde{\mathcal{C}}_s = \frac{N-1}{M(N-M)} [N^2 \mathcal{C}^{(M)} - M^2 \mathcal{C}]. \quad (15)$$

If $T \gtrsim J$, where we can assume only spin correlations up to next-nearest neighbors contribute, Eq. (15) then gives a combination of $\mathcal{C}(0, 0)$, $\mathcal{C}(1, 0)$, and $\mathcal{C}(1, 1)$. $\mathcal{C}(0, 0)$ is related to \mathcal{D} via $\mathcal{C}(0, 0) = (N-1) \langle n \rangle - 2\mathcal{D}$, so it can be measured independently as previously discussed, while $\mathcal{C}(1, 0)$ can be measured independently using the singlet-triplet oscillation method [16,17]. With these measurements and Eq. (15) $\mathcal{C}(1, 1)$ can be resolved.

A major goal in strongly correlated matter is to understand the consequences of doping Mott insulators and magnetically ordered phases. Our results provide a useful starting point for the exploration of the doped SU(3) FHM at finite temperature. This has been an active area in the past few years for SU(2) ultracold FHMs. One example of progress is the development and testing of geometric string theory [18,24,61–67], which draws a connection between the strongly correlated quantum states at finite doping and the AFM parent state at 1/2-filling. Reference [18] found that for $N = 2$ the geometric string

patterns are observable at $T \lesssim J$ and upon $\lesssim 10\%$ doping. These temperatures have been attained with AEAs in OLs and therefore the exploration of the doped SU(3) FHM is a timely question. Our results at 1/3-filling exhibit interesting magnetic crossovers around $T^* = 0.57J$, and we expect this to drive qualitative changes in the string length and anisotropy across this crossover.

ACKNOWLEDGMENTS

Authors would like to thank useful discussions with Yoshiro Takahashi, Shintaro Taie, Henning Schlömer, and Sohail Dasgupta. E.I.G.P., R.T.S., and E.K. are supported by the Grant DE-SC-0022311, funded by the U.S. Department of Energy, Office of Science. We acknowledge support from the Robert A. Welch Foundation (C-1872), the National Science Foundation (PHY-1848304), and the W. F. Keck Foundation (Grant No. 995764). Computing resources were supported in part by the Big-Data Private-Cloud Research Cyberinfrastructure MRI-award funded by NSF under Grant No. CNS-1338099 and by Rice University's Center for Research Computing (CRC), as well as the Spartan high-performance computing facility at San José State University supported by the NSF under Grant No. OAC-1626645. K.R.A.H.'s contribution benefited from discussions at the Aspen Center for Physics, supported by the National Science Foundation Grant No. PHY-1066293, and the KITP, which was supported in part by the National Science Foundation under Grant No. PHY-1748958.

APPENDIX A: INTERACTION ENERGY DERIVATIVE

Figure 7 shows the derivative of the interaction energy $P = UD$ with respect to temperature, dP/dT . Here, we observe that only for $U/t > 6$ does dP/dT exhibit a clear sharp dip when temperature increases at low temperatures. For those interaction strengths, we define T^*/t as the temperature at

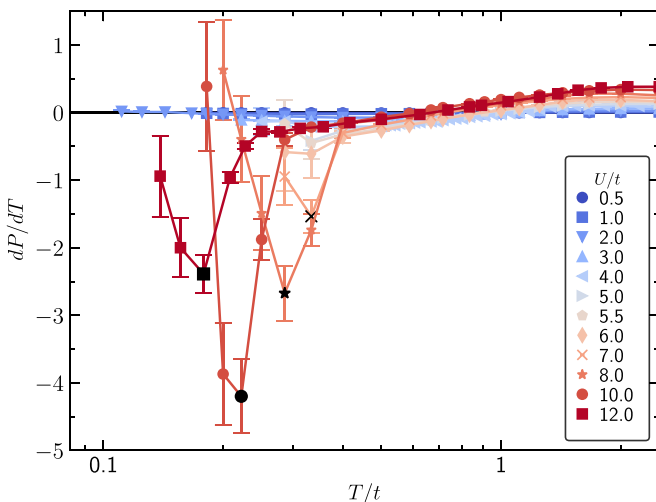


FIG. 7. Derivative of the interaction energy $P = UD$ with respect to temperature $d(UD)/dT$ vs T/t . Results are presented for different U/t . Black markers correspond to T^*/t , which are obtained by locating the minima of dP/dT for $U/t > 5$. Solid markers are DQMC data and lines connect the dots to guide the eye.

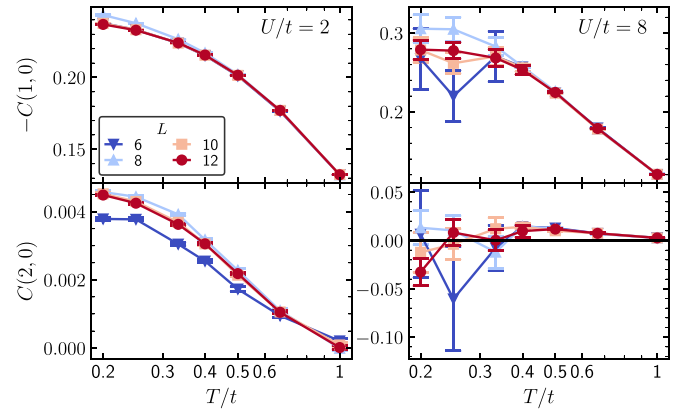


FIG. 8. Finite-size analysis. Spin correlators as a function of T/t are presented for $U/t = 2$ and $U/t = 8$ at system sizes: 6×6 , 8×8 , 10×10 , and 12×12 .

which the minima of dP/dT is located and we indicate them with black markers in this figure. They are shown as a function of U/t in the inset of Fig. 6.

APPENDIX B: FINITE-SIZE EFFECTS

In Fig. 5 we presented \mathcal{D} and $C(1, 1)$ for $L \times L$ systems with $L = 6, 8, 10, 12$. In Fig. 8 we present $C(1, 0)$ and $C(2, 0)$ for completeness. For $U/t = 2$, $C(1, 0) < 0$ and is well converged at all temperatures already for $L = 6$. For $C(2, 0)$, finite-size effects are minimal for 8×8 lattices and the value of the correlation always remains positive but very small. On the other hand for $U/t = 8$, both spin correlators are well converged for $T > 0.4$, but finite-size errors are present for 6×6 lattices at $T/t < 0.4$. At this interaction, $C(1, 0) < 0$ for all system sizes and is well converged for $L = 10$ and 12 . Finally, $C(2, 0)$ requires further statistics to be resolved at the lowest temperatures, which are inaccessible to our current numerical capabilities.

APPENDIX C: ANALYSIS OF TROTTER ERROR

The density of on-site pairs \mathcal{D} has historically been found to be one of the most sensitive quantities to the systematic

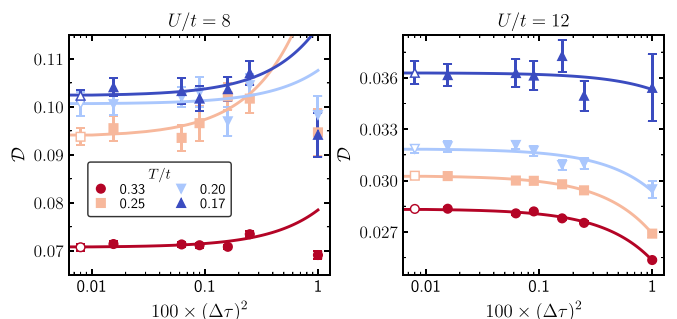


FIG. 9. Density of on-site pairs as a function of $(\Delta\tau)^2$. Results are presented for different T/t for $U/t = 8$ and $U/t = 12$. Solid markers indicate DQMC results, solid lines correspond to linear fits to the data, and open markers are the $\Delta\tau \rightarrow 0$ extrapolation obtained from the fit.

Trotter error [68]. In order to support the claims derived from the low-temperature behavior observed at large U/t we analyze the Trotter error by comparing the results obtained for \mathcal{D} with $\Delta\tau = 0.0125/t, 0.025/t, 0.03/t, 0.04/t, 0.05/t,$

and $0.1/t$ at $T/t = 0.17, 0.2, 0.25,$ and 0.33 for $U/t = 8$ and 12 . These are presented in Fig. 9. In all cases, the $\Delta\tau \rightarrow 0$ extrapolation leads to a correction no larger than $\sim 5\%$, much smaller than the low-temperature rise of \mathcal{D} for $U > U_c$.

-
- [1] Y. Tokura, Orbital physics in transition-metal oxides, *Science* **288**, 462 (2000).
- [2] T. A. Tóth, A. M. Läuchli, F. Mila, and K. Penc, Three-sublattice ordering of the SU(3) Heisenberg model of three-flavor fermions on the square and cubic lattices, *Phys. Rev. Lett.* **105**, 265301 (2010).
- [3] B. Bauer, P. Corboz, A. M. Läuchli, L. Messio, K. Penc, M. Troyer, and F. Mila, Three-sublattice order in the SU(3) Heisenberg model on the square and triangular lattice, *Phys. Rev. B* **85**, 125116 (2012).
- [4] M. Hermele, V. Gurarie, and A. M. Rey, Mott insulators of ultracold fermionic alkaline earth atoms: Underconstrained magnetism and chiral spin liquid, *Phys. Rev. Lett.* **103**, 135301 (2009).
- [5] M. Hermele and V. Gurarie, Topological liquids and valence cluster states in two-dimensional SU(N) magnets, *Phys. Rev. B* **84**, 174441 (2011).
- [6] P. Nataf and F. Mila, Exact diagonalization of Heisenberg SU(N) models, *Phys. Rev. Lett.* **113**, 127204 (2014).
- [7] P. Corboz, A. M. Läuchli, K. Penc, M. Troyer, and F. Mila, Simultaneous dimerization and SU(4) symmetry breaking of 4-color fermions on the square lattice, *Phys. Rev. Lett.* **107**, 215301 (2011).
- [8] C. Wu, Hidden symmetry and quantum phases in spin-3/2 cold atomic systems, *Mod. Phys. Lett. B* **20**, 1707 (2006).
- [9] M. A. Cazalilla, A. F. Ho, and M. Ueda, Ultracold gases of ytterbium: Ferromagnetism and Mott states in an SU(6) Fermi system, *New J. Phys.* **11**, 103033 (2009).
- [10] A. V. Gorshkov, M. Hermele, V. Gurarie, C. Xu, P. S. Julienne, J. Ye, P. Zoller, E. Demler, M. D. Lukin, and A. M. Rey, Two-orbital SU(N) magnetism with ultracold alkaline-earth atoms, *Nature Phys.* **6**, 289 (2010).
- [11] M. A. Cazalilla and A. M. Rey, Ultracold Fermi gases with emergent SU(N) symmetry, *Rep. Prog. Phys.* **77**, 124401 (2014).
- [12] S. Stellmer, F. Schreck, and T. C. Killian, Degenerate quantum gases of strontium, in *Annual Review of Cold Atoms and Molecules* (World Scientific, Singapore, 2014), Chap. 1, pp. 1–80.
- [13] S. Taie, R. Yamazaki, S. Sugawa, and Y. Takahashi, An SU(6) Mott insulator of an atomic Fermi gas realized by large-spin Pomeranchuk cooling, *Nature Phys.* **8**, 825 (2012).
- [14] C. Hofrichter, L. Riegger, F. Scazza, M. Höfer, D. R. Fernandes, I. Bloch, and S. Fölling, Direct probing of the Mott crossover in the SU(N) Fermi-Hubbard model, *Phys. Rev. X* **6**, 021030 (2016).
- [15] D. Tusi, L. Franchi, L. F. Livì, K. Baumann, D. B. Orenes, L. D. Re, R. E. Barfknecht, T. Zhou, M. Inguscio, G. Cappellini, M. Capone, J. Catani, and L. Fallani, Flavour-selective localization in interacting lattice fermions, *Nature Phys.* **18**, 1201 (2022).
- [16] H. Ozawa, S. Taie, Y. Takasu, and Y. Takahashi, Antiferromagnetic spin correlation of SU(N) Fermi gas in an optical superlattice, *Phys. Rev. Lett.* **121**, 225303 (2018).
- [17] S. Taie, E. Ibarra-García-Padilla, N. Nishizawa, Y. Takasu, Y. Kuno, H.-T. Wei, R. T. Scalettar, K. R. A. Hazzard, and Y. Takahashi, Observation of antiferromagnetic correlations in an ultracold SU(N) Hubbard model, *Nature Phys.* **18**, 1356 (2022).
- [18] C. S. Chiu, G. Ji, A. Bohrdt, M. Xu, M. Knap, E. Demler, F. Grusdt, M. Greiner, and D. Greif, String patterns in the doped Hubbard model, *Science* **365**, 251 (2019).
- [19] E. Altman, K. R. Brown, G. Carleo, L. D. Carr, E. Demler, C. Chin, B. DeMarco, S. E. Economou, M. A. Eriksson, Kai-Mei C. Fu, M. Greiner, K. R. A. Hazzard, R. G. Hulet, A. J. Kollár, B. L. Lev, M. D. Lukin, R. Ma, X. Mi, S. Misra, C. Monroe, K. Murch, Z. Nazario, K.-K. Ni, A. C. Potter, P. Roushan, M. Saffman, M. Schleier-Smith, I. Siddiqi, R. Simmonds, M. Singh, I. B. Spielman, K. Temme, D. S. Weiss, J. Vučković, V. Vuletić, J. Ye, and M. Zwierlein, Quantum simulators: Architectures and opportunities, *PRX Quantum* **2**, 017003 (2021).
- [20] C. Gross and I. Bloch, Quantum simulations with ultracold atoms in optical lattices, *Science* **357**, 995 (2017).
- [21] I. Bloch, J. Dalibard, and S. Nascimbène, Quantum simulations with ultracold quantum gases, *Nature Phys.* **8**, 267 (2012).
- [22] M. F. Parsons, A. Mazurenko, C. S. Chiu, G. Ji, D. Greif, and M. Greiner, Site-resolved measurement of the spin-correlation function in the Fermi-Hubbard model, *Science* **353**, 1253 (2016).
- [23] A. Mazurenko, C. S. Chiu, G. Ji, M. F. Parsons, M. Kanász-Nagy, R. Schmidt, F. Grusdt, E. Demler, D. Greif, and M. Greiner, A cold-atom Fermi-Hubbard antiferromagnet, *Nature (London)* **545**, 462 (2017).
- [24] J. Koeppell, D. Bourgund, P. Sompet, S. Hirthe, A. Bohrdt, Y. Wang, F. Grusdt, E. Demler, G. Salomon, C. Gross, and I. Bloch, Microscopic evolution of doped Mott insulators from polaronic metal to Fermi liquid, *Science* **374**, 82 (2021).
- [25] T. Hartke, B. Oreg, N. Jia, and M. Zwierlein, Doublon-hole correlations and fluctuation thermometry in a Fermi-Hubbard gas, *Phys. Rev. Lett.* **125**, 113601 (2020).
- [26] G. Ji, M. Xu, L. H. Kendrick, C. S. Chiu, J. C. Brüggengjürgen, D. Greif, A. Bohrdt, F. Grusdt, E. Demler, M. Lebrat, and M. Greiner, Coupling a mobile hole to an antiferromagnetic spin background: Transient dynamics of a magnetic polaron, *Phys. Rev. X* **11**, 021022 (2021).
- [27] R. Yamamoto, J. Kobayashi, T. Kuno, K. Kato, and Y. Takahashi, An ytterbium quantum gas microscope with narrow-line laser cooling, *New J. Phys.* **18**, 023016 (2016).
- [28] F. Schäfer, T. Fukuhara, S. Sugawa, Y. Takasu, and Y. Takahashi, Tools for quantum simulation with ultracold atoms in optical lattices, *Nature Rev. Phys.* **2**, 411 (2020).
- [29] D. Okuno, Y. Amano, K. Enomoto, N. Takei, and Y. Takahashi, Schemes for nondestructive quantum gas microscopy of single atoms in an optical lattice, *New J. Phys.* **22**, 013041 (2020).
- [30] A. Sotnikov, Critical entropies and magnetic-phase-diagram analysis of ultracold three-component fermionic mixtures in optical lattices, *Phys. Rev. A* **92**, 023633 (2015).

- [31] A. Sotnikov and W. Hofstetter, Magnetic ordering of three-component ultracold fermionic mixtures in optical lattices, *Phys. Rev. A* **89**, 063601 (2014).
- [32] H. Yanatori and A. Koga, Finite-temperature phase transitions in the $SU(N)$ Hubbard model, *Phys. Rev. B* **94**, 041110(R) (2016).
- [33] E. Ibarra-García-Padilla, S. Dasgupta, H.-T. Wei, S. Taie, Y. Takahashi, R. T. Scalettar, and K. R. A. Hazzard, Universal thermodynamics of an $SU(N)$ Fermi-Hubbard model, *Phys. Rev. A* **104**, 043316 (2021).
- [34] W. Nie, D. Zhang, and W. Zhang, Ferromagnetic ground state of the $SU(3)$ Hubbard model on the Lieb lattice, *Phys. Rev. A* **96**, 053616 (2017).
- [35] M. Hafez-Torbati and W. Hofstetter, Artificial $SU(3)$ spin-orbit coupling and exotic Mott insulators, *Phys. Rev. B* **98**, 245131 (2018).
- [36] M. Hafez-Torbati and W. Hofstetter, Competing charge and magnetic order in fermionic multicomponent systems, *Phys. Rev. B* **100**, 035133 (2019).
- [37] M. Hafez-Torbati, J.-H. Zheng, B. Irsigler, and W. Hofstetter, Interaction-driven topological phase transitions in fermionic $SU(3)$ systems, *Phys. Rev. B* **101**, 245159 (2020).
- [38] A. Pérez-Romero, R. Franco, and J. Silva-Valencia, Phase diagram of the $SU(3)$ Fermi Hubbard model with next-neighbor interactions, *Eur. Phys. J. B* **94**, 229 (2021).
- [39] C. Honerkamp and W. Hofstetter, Ultracold fermions and the $SU(N)$ Hubbard Model, *Phys. Rev. Lett.* **92**, 170403 (2004).
- [40] C. Romen and A. M. Läuchli, Structure of spin correlations in high-temperature $SU(N)$ quantum magnets, *Phys. Rev. Res.* **2**, 043009 (2020).
- [41] R. Blankenbecler, D. J. Scalapino, and R. L. Sugar, Monte Carlo calculations of coupled boson-fermion systems. I, *Phys. Rev. D* **24**, 2278 (1981).
- [42] S. Sorella, S. Baroni, R. Car, and M. Parrinello, A novel technique for the simulation of interacting fermion systems, *Europhys. Lett.* **8**, 663 (1989).
- [43] M. Rigol, T. Bryant, and R. R. P. Singh, Numerical linked-cluster approach to quantum lattice models, *Phys. Rev. Lett.* **97**, 187202 (2006).
- [44] B. Tang, E. Khatami, and M. Rigol, A short introduction to numerical linked-cluster expansions, *Comput. Phys. Commun.* **184**, 557 (2013).
- [45] The Manhattan distance between two points is the sum of the absolute differences of their Cartesian coordinates.
- [46] E. Ibarra-García-Padilla, R. Mukherjee, R. G. Hulet, K. R. A. Hazzard, T. Paiva, and R. T. Scalettar, Thermodynamics and magnetism in the two-dimensional to three-dimensional crossover of the Hubbard model, *Phys. Rev. A* **102**, 033340 (2020).
- [47] R. A. Hart, P. M. Duarte, T.-L. Yang, X. Liu, T. Paiva, E. Khatami, R. T. Scalettar, N. Trivedi, D. A. Huse, and R. G. Hulet, Observation of antiferromagnetic correlations in the Hubbard model with ultracold atoms, *Nature (London)* **519**, 211 (2015).
- [48] D. Greif, T. Uehlinger, G. Jotzu, L. Tarruell, and T. Esslinger, Short-range quantum magnetism of ultracold fermions in an optical lattice, *Science* **340**, 1307 (2013).
- [49] L. W. Cheuk, M. A. Nichols, K. R. Lawrence, M. Okan, H. Zhang, E. Khatami, N. Trivedi, T. Paiva, M. Rigol, and M. W. Zwierlein, Observation of spatial charge and spin correlations in the 2D Fermi-Hubbard model, *Science* **353**, 1260 (2016).
- [50] P. T. Brown, D. Mitra, E. Guardado-Sanchez, P. Schauß, S. S. Kondov, E. Khatami, T. Paiva, N. Trivedi, D. A. Huse, and W. S. Bakr, Spin-imbalance in a 2D Fermi-Hubbard system, *Science* **357**, 1385 (2017).
- [51] P. T. Brown, D. Mitra, E. Guardado-Sanchez, R. Nourafkan, A. Reymbaut, C.-D. Hébert, S. Bergeron, A.-M. S. Tremblay, J. Kokalj, D. A. Huse, P. Schauß, and W. S. Bakr, Bad metallic transport in a cold atom Fermi-Hubbard system, *Science* **363**, 379 (2019).
- [52] M. A. Nichols, L. W. Cheuk, M. Okan, T. R. Hartke, E. Mendez, T. Senthil, E. Khatami, H. Zhang, and M. W. Zwierlein, Spin transport in a Mott insulator of ultracold fermions, *Science* **363**, 383 (2019).
- [53] R. T. Scalettar, R. M. Noack, and R. R. P. Singh, Ergodicity at large couplings with the determinant Monte Carlo algorithm, *Phys. Rev. B* **44**, 10502 (1991).
- [54] These global moves update, at a given lattice site, all the imaginary time slices that couple two spin flavors.
- [55] C. Feng, E. Ibarra-García-Padilla, K. R. A. Hazzard, R. T. Scalettar, S. Zhang, and E. Vitali, Metal-insulator transition and quantum magnetism in the $SU(3)$ Fermi-Hubbard model: Dientangling nesting and the Mott transition, [arXiv:2306.16464](https://arxiv.org/abs/2306.16464).
- [56] D. Garwood, J. Mongkolkiattichai, L. Liu, J. Yang, and P. Schauss, Site-resolved observables in the doped spin-imbalance triangular Hubbard model, *Phys. Rev. A* **106**, 013310 (2022).
- [57] J. Kokalj and R. H. McKenzie, Thermodynamics of a bad metal–Mott insulator transition in the presence of frustration, *Phys. Rev. Lett.* **110**, 206402 (2013).
- [58] We tested the method for the half-filled $SU(2)$ FHM in the honeycomb lattice where $U_c/t \sim 3.8$ (3.87 from Ref. [69] and 3.78 from Ref. [70]). This method is consistent with the results, predicting $U_c/t = 3.9 \pm 0.2$. Although these results partially support the validity of the analysis in the present study, this technique is not perfectly reliable, for example, it gives a finite U_c in the $SU(2)$ square lattice case, and so confirmation with other techniques is advised (such as CPQMC as in this case).
- [59] G. Pasqualetti, O. Bettermann, N. D. Opong, E. Ibarra-García-Padilla, S. Dasgupta, R. T. Scalettar, K. R. A. Hazzard, I. Bloch, and S. Fölling, Equation of state and thermometry of the 2D $SU(N)$ Fermi-Hubbard model, [arXiv:2305.18967](https://arxiv.org/abs/2305.18967).
- [60] Q. Zhou and T.-L. Ho, Universal thermometry for quantum simulation, *Phys. Rev. Lett.* **106**, 225301 (2011).
- [61] F. Grusdt, M. Kánasz-Nagy, A. Bohrdt, C. S. Chiu, G. Ji, M. Greiner, D. Greif, and E. Demler, Parton theory of magnetic polarons: Mesonic resonances and signatures in dynamics, *Phys. Rev. X* **8**, 011046 (2018).
- [62] F. Grusdt, A. Bohrdt, and E. Demler, Microscopic spin-charge theory of magnetic polarons in the t - J model, *Phys. Rev. B* **99**, 224422 (2019).
- [63] A. Bohrdt, E. Demler, F. Pollmann, M. Knap, and F. Grusdt, Parton theory of angle-resolved photoemission spectroscopy spectra in antiferromagnetic Mott insulators, *Phys. Rev. B* **102**, 035139 (2020).
- [64] A. Bohrdt, F. Grusdt, and M. Knap, Dynamical formation of a magnetic polaron in a two-dimensional quantum antiferromagnet, *New J. Phys.* **22**, 123023 (2020).

- [65] A. Bohrdt, Y. Wang, J. Koepsell, M. Kánasz-Nagy, E. Demler, and F. Grusdt, Dominant fifth-order correlations in doped quantum antiferromagnets, *Phys. Rev. Lett.* **126**, 026401 (2021).
- [66] A. Bohrdt, L. Homeier, I. Bloch, E. Demler, and F. Grusdt, Strong pairing in mixed-dimensional bilayer antiferromagnetic Mott insulators, *Nature Phys.* **18**, 651 (2022).
- [67] F. Grusdt, E. Demler, and A. Bohrdt, Pairing of holes by confining strings in antiferromagnets, *SciPost Phys.* **14**, 090 (2023).
- [68] C.-C. Chang, R. T. Scalettar, E. V. Gorelik, and N. Blümer, Discriminating antiferromagnetic signatures in systems of ultracold fermions by tunable geometric frustration, *Phys. Rev. B* **88**, 195121 (2013).
- [69] S. Sorella, Y. Otsuka, and S. Yunoki, Absence of a spin liquid phase in the Hubbard model on the honeycomb lattice, *Sci. Rep.* **2**, 992 (2012).
- [70] F. F. Assaad and I. F. Herbut, Pinning the order: The nature of quantum criticality in the Hubbard model on honeycomb lattice, *Phys. Rev. X* **3**, 031010 (2013).